Diffusion Transformer Model With Compact Prior for Low-dose PET Reconstruction

Bin Huang[1], Xubiao Liu[2], Lei Fang[4], Qiegen Liu[2,*], Bingxuan Li[3,*]

[1] School of Mathematics and Computer Sciences, Nanchang University, Nanchang, China
[2] School of Information Engineering, Nanchang University, Nanchang, China
[3] Institute of Artificial Intelligence, Hefei Comprehensive National Science Center, Hefei, China
[4] Department of Biomedical Engineering, Huazhong University of Science and Technology, Wuhan, China
[*] Author to whom any correspondence should be addressed.

E-mail: liuqiegen@ncu.edu.cn and libingxuan@iai.ustc.edu.cn

Keywords: low-dose PET, diffusion transformer model, data consistency, joint compact prior

Abstract

Objective. Positron emission tomography (PET) is an advanced medical imaging technique that plays a crucial role in non-invasive clinical diagnosis. However, while reducing radiation exposure through low-dose PET scans is beneficial for patient safety, it often results in insufficient statistical data. This scarcity of data poses significant challenges for accurately reconstructing high-quality images, which are essential for reliable diagnostic outcomes. *Approach.* In this research, we propose a diffusion transformer model (DTM) guided by joint compact prior (JCP) to enhance the reconstruction quality of low-dose PET imaging. In light of current research findings, we present a pioneering PET reconstruction model that integrates diffusion and transformer models for joint optimization. This model combines the powerful distribution mapping abilities of diffusion model with the capacity of transformers to capture long-range dependencies, offering significant advantages for low-dose PET reconstruction. Additionally, the incorporation of the lesion refining block and alternating direction method of multipliers (ADMM) enhance the recovery capability of lesion regions and preserves detail information, solving blurring problems in lesion areas and texture details of most deep learning frameworks. *Main results*. Experimental results validate the effectiveness of DTM in reconstructing low-dose PET image quality. DTM achieves state-of-the-art performance across various metrics, including PSNR, SSIM, NRMSE, CR, and COV, demonstrating its ability to reduce noise while preserving critical clinical details such as lesion structure and texture. Compared with baseline methods, DTM delivers best results in denoising and lesion preservation across various low-dose levels, including 10%, 25%, 50%, and even ultra-low-dose level such as 1%. DTM shows robust generalization performance on phantom and patient datasets, highlighting its adaptability to varying imaging conditions. *Significance*. This approach reduces radiation exposure while ensuring reliable imaging for early disease detection and clinical decision-making, offering a promising tool for both clinical and research applications.

1. Introduction

Positron emission tomography (PET) is a highly sensitive and widely utilized functional imaging modality employed in the diagnosis, staging, and treatment monitoring of various diseases, including malignant tumors, neurological disorders, and cardiovascular conditions [1-3]. This imaging technique allows for the visualization and quantification of metabolic processes in the body, providing critical information that is essential for accurate medical decision-making [4]. Despite its invaluable role in clinical practice, PET imaging has the inherent drawback of exposing patients to ionizing radiation. This exposure poses significant health risks, particularly for vulnerable populations such as pediatric patients and individuals requiring frequent diagnostic procedures [5-7]. Consequently, reducing the radiation dose in PET imaging is a crucial objective to minimize these risks [8]. However, reducing the dose typically results in increased noise and compromised image quality, creating significant challenges for accurate clinical interpretation [9]. The elevated noise levels in low-dose PET images can obscure critical diagnostic details, leading to potential misdiagnosis or the need for repeat scans, which defeats the purpose of dose reduction [10]. Therefore, there is a pressing need to develop advanced image reconstruction techniques that can enhance the quality of low-dose PET images while maintaining diagnostic accuracy [11].

While traditional denoising methods like Gaussian denoising [12], total variation (TV) [13-14], and non-local means (NLM) [15-16] have been utilized for low-dose PET imaging, undoubtedly, recent advancements in deep learning techniques have shown impressive performance. In recent years, the advent of deep learning has revolutionized the field of medical imaging, offering new avenues for improving image quality of PET reconstruction. Deep learning approaches [17-18], particularly convolutional neural networks (CNNs), have demonstrated remarkable success in various image processing tasks due to their ability to learn complex patterns and features from large datasets. For instance, Gong *et al.* [19] developed a deep learning-based approach to enhance the quality of low-dose PET images by training a CNN to map low-dose images to their full-dose counterparts, significantly reducing noise and improving image clarity. Similarly, Xu *et al.* [20] proposed an encoder-decoder residual CNN framework with

Co-first Authors: B. Huang and X. Liu. Corresponding Authors: Q. Liu and B. Li

concatenate skip connections that yielded satisfactory results at significantly low dose. Other deep learning methods have also shown promise in PET image reconstruction. For example, Peng *et al.* [21] applied a deep learning-based denoising method to low-dose PET images, achieving substantial noise reduction while preserving important image details by incorporating CT information. Gong *et al.* [22] introduced a deep neural network for PET image denoising by using simulation data and fine-tune the last few layers of the network using real data sets. Furthermore, Zhou *et al.* [23] utilized a cycle-consistent GAN (Cycle GAN) to translate low-dose PET images to high-dose equivalents, yielding impressive results in terms of image fidelity and diagnostic quality. Pan *et al.* [24] have demonstrated notable efficacy in the reconstruction of low-dose PET utilizing the contemporary diffusion model.

With the advancement of deep learning, both diffusion models and transformer models have demonstrated significant promise in the field of PET low-dose image reconstruction. The objective of PET low-dose imaging is to reduce the radiation exposure to patients while maintaining image quality, which poses substantial challenges. Deep learning techniques, particularly diffusion models and transformer models, have shown effectiveness in addressing these challenges by enhancing image quality and preserving essential diagnostic details. Diffusion models, which are generative models that learn the underlying data distribution by simulating the diffusion process, have recently gained attention for their ability to denoise and enhance PET images. Gong *et al.* [25] demonstrated the potential of using denoising diffusion probabilistic models to reduce noise in PET images, showing that employing MR prior as the network input while embedding PET image as a data-consistency constraint can achieve better performance. Similarly, Jiang *et al.* [26] proposed an unsupervised PET enhancement approach based on latent diffusion models, which effectively enhanced PET images with latent information. In visual comparisons, uPETe demonstrated superior performance in preserving fine organ structures, such as clear tissue boundaries in both axial and coronal views, with minimal noise artifacts. Another notable contribution by Xie *et al.* [27] involved a dose-aware diffusion model tailored for 3D low-dose PET denoising, validated through multi-institutional studies and real low-dose data. Transformer models, on the other hand, have been widely recognized for their ability to capture long-range dependencies and process large-scale data efficiently. In the context of medical imaging, transformer models have been leveraged to improve PET image reconstruction by exploiting their powerful feature extraction and representation capabilities. Zhang *et al.* [28] introduced the spatial adaptive and transformer fusion network (STFNet) for low-count PET blind denoising with MRI. STFNet demonstrated an exceptional ability to enhance low-count PET images by retaining sharp edges and accurate textures, with MRI input further improving subtle contrast in regions such as cortical structures. Additionally, Luo *et al.* [29] developed a 3D transformer-GAN for high-quality PET reconstruction, combining CNNs and transformers with a lightweight design. This model successfully mitigated reconstruction artifacts, particularly in complex regions like the brain, where it restored clear cortical folds and enhanced the visibility of fine details. Hu and Liu [30] presented TransEM, a residual Swin-transformer-based regularized PET image reconstruction method, which further validated the advantages of transformers in PET imaging. TransEM effectively captured long-range dependencies and fine local structures, such as detailed cortical boundaries, while minimizing noise and maintaining structural consistency in low-dose reconstructions.

Given the complementary strengths of diffusion and transformer models, there is a growing interest in integrating these approaches to leverage their respective advantages. By combining the iterative refinement capabilities of diffusion models with the rapid processing power of transformer models, it is possible to achieve enhanced reconstruction outcomes for PET low-dose imaging.

In this study, we have proposed a novel diffusion transformer model for low-dose PET reconstruction, called DTM. Specifically, horizontal and vertical compact priors, called joint compact prior (JCP), are extracted from normal-dose PET. This JCP will guide the training process of DTM. DTM comprises both transformer and diffusion stages. During reconstruction procedure, the lesion refining block is seamlessly integrated with alternating direction method of multipliers (ADMM) to heighten fidelity. This block will identify lesion locations by selecting high-value regions. By leveraging data consistency stage (DCS) to govern the generation process of normal-dose PET, the lesion refining block not only bolsters model interpretability but also ensures the preservation of authenticity and reliability, thereby further enhancing its overall performance.

The theoretical and practical contributions of this work are summarized as follows:

- Integration of diffusion and transformer stages for low-dose PET reconstruction significantly enhances the model's ability to generate normal-dose PET. While the diffusion model enhances the detail reconstruction capability, the transformer model introduces multi-head attention mechanism and global information which makes DTM achieves remarkable reconstruction results.
- Implementation of a lesion refining block will perform targeted reconstruction specifically tailored to these lesions within DCS. By integrating this block with ADMM algorithm, we significantly enhance the recovery capability of lesion regions, achieving positive strides in lesion recovery.
- Introduction of the JCP extraction block allows simultaneous extraction of horizontal and vertical compact priors from normal-dose PET. The diffusion process only needs to predict JCP instead of the entire normal-dose data. This JCP refers to latent information that significantly reduces computational complexity and shortens the reconstruction time required.

The rest of the manuscript is organized as follows. Relevant background on score-based diffusion model is demonstrated in Section II. Detailed procedure and algorithm of the proposed method are presented in Section III. Experimental results and specifications about the implementation and experiments are given in Section IV. At last, conclusion is drawn in Section V.

2. Preliminary

2.1. Vision Transformers

The transformer model, initially developed for natural language processing tasks, has been adapted for various vision tasks including image recognition, segmentation, and object detection. Vision transformers [31] decompose images into sequences of patches, enabling them to learn relationships between patches effectively. These models exhibit a notable ability to capture long-range dependencies between sequences of image patches and adapt to varying input content [32]. Consequently, transformer models have been explored for low-level vision tasks such as super-resolution, image colorization, denoising, and deraining. However, the self-attention mechanism in transformers can lead to quadratic increases in computational complexity with the number of image patches, limiting its application to high-resolution images. To address this challenge, recent methods for low-level image processing adopt alternative strategies to mitigate complexity. One approach involves employing self-attention within local image regions [33-34] using the Swin transformer design [34]. However, this approach restricts context aggregation to local neighborhoods, deviating from the primary motivation behind utilizing self-attention over convolutions and rendering it less suitable for image restoration tasks.

2.2. Diffusion Models

Diffusion models have emerged as frontrunners in both density estimation [35] and sample quality enhancement [36]. These models utilize parameterized Markov chains to optimize the lower variational bound on the likelihood function, enabling them to generate target distributions with greater accuracy compared to alternative generative models.

The diffusion process operates on an input image x_0, gradually transforming it into Gaussian noise $x_t \sim \mathcal{N}(0, I)$ through t iterations. Each iteration of this process is described as follows:

$$q(x_t|x_{t-1}) = \mathcal{N}(x_t; \sqrt{1-\beta_t}x_{t-1}, \beta_t I) \tag{1}$$

where x_t denotes the noised image at time-step t, β_t represents the predefined scale factor, and $\mathcal{N}$ represents the Gaussian distribution. During the reverse process, diffusion models sample a Gaussian random noise map x_t, then progressively denoise x_t until it achieves a high-quality output x_0:

$$p(x_{t-1}|x_t, x_0) = \mathcal{N}(x_{t-1}; \mu_t(x_t, x_0), \sigma_t^2 I) \tag{2}$$

To train a denoising network $\epsilon_\theta(x_t, t)$, given a clean image x_0, diffusion models randomly sample a time step t and a noise $\epsilon \sim \mathcal{N}(0, I)$ to generate noisy images x_t according to Eq. (2).

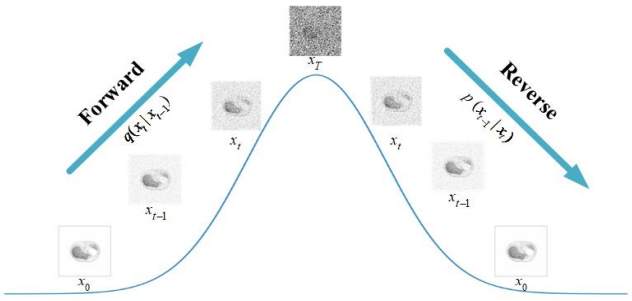

Fig. 1. Forward and reverse processes of DDPM.

3. Proposed Method

Diffusion model and transformer model each offer unique advantages: diffusion models can fully and efficiently use the powerful distribution mapping abilities to generate images, while transformer models can model long-range pixel dependencies. To effectively combine these two models, it is necessary to make appropriate modifications. Traditional diffusion models require extensive iterative processes, resulting in long training and execution times. Conversely, transformer U-net deliver results rapidly. To merge these models, we can alter the training target of the diffusion model from complete image data to compact priors. This adjustment substantially reduces the training and iteration time for diffusion models, thereby enabling the integration of the two models, as demonstrated in the study by [37].

Inspired by DiffIR [37], we propose a JCP tailored for PET imaging. The JCP serves as a guiding mechanism for the transformer, leveraging the strengths of both the diffusion model and the transformer model to achieve superior reconstruction outcomes. A common challenge in many deep learning models is that noise removal mechanisms may inadvertently lead to the blurring of detailed information and lesion areas. To effectively mitigate this issue, we integrate a lesion refining block with ADMM algorithm. This integration significantly enhances the recovery capability of lesion regions and preserves detailed information, representing a positive stride towards addressing this challenge.

3.1. DTM

In summary, DTM consists of four parts: JCP extraction, prior prediction via diffusion process, feeding prior and PET images into

transformer stage, and fidelity enhancement using lesion refining block and ADMM block. Initially, a compact prior extraction block is proposed to extract JCP, composed of horizontal prior and vertical prior, from normal-dose PET to guide subsequent low-dose PET reconstruction. This block comprises stacked residual blocks and linear layers.

In the diffusion stage, denoised horizontal and vertical compact priors are predicted by the diffusion process. The diffusion module predicts specific noise through conditional diffusion. The estimated degraded prior is then inputted to the transformer module as affine transformation parameters to reconstruct high-quality normal-dose PET.

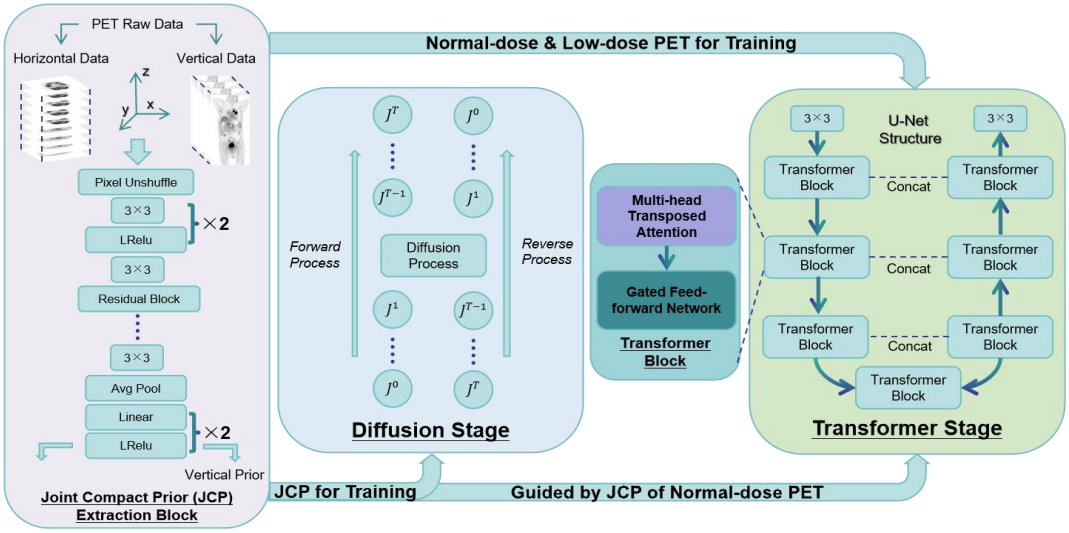

Fig. 2. The pipeline of DTM training procedure. DTM mainly consists by JCP extraction block, diffusion stage and transformer stage. The horizontal prior and vertical prior are combined to a JCP which will be feed into the diffusion stage to predict and guide transformer stage to reconstruct final result.

In the transformer stage, multiple transformer blocks are combined in a U-net form, with each block incorporating a multi-head transposed attention and a gated feed-forward network. The transformer module captures distant pixel interactions, where the multi-head transposed attention module aggregates local and non-local pixel interactions, indicating its ability to perform feature interaction across channels. The gated feed-forward network suppresses less informative features, allowing only useful information to further pass through the network hierarchy. Finally, transformer exploits JCP to restore normal-dose PET from low-dose PET.

3.2. Training Procedure

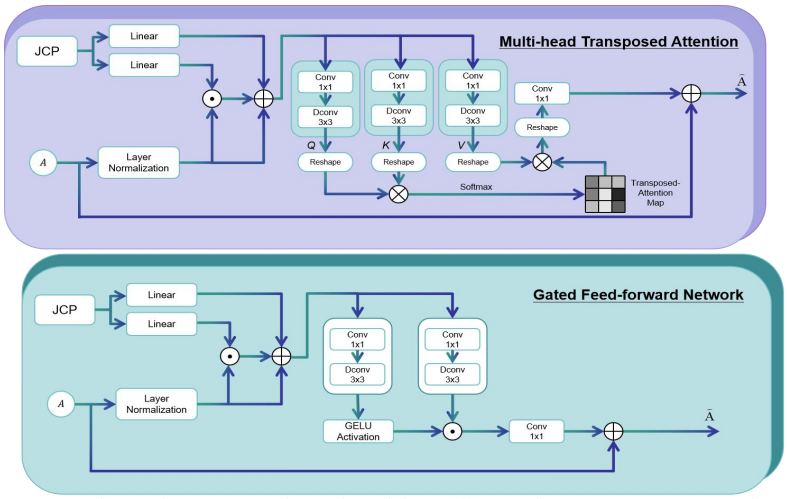

Fig. 3. Pipelines of Multi-head Transposed Attention (MTA) and Gated Feed-forward Network (GFN). MTA captures dependencies using Q, K, V transformations and attention maps. GFN refines features with convolutions, activation, and gating for robust learning.

The pipeline of DTM training procedure is shown in Fig. 2. This procedure involves JCP extraction block, diffusion stage and the transformer stage. During the training phase, the normal-dose JCP is utilized by the diffusion stage for training. Simultaneously, the transformer stage requires paired normal-dose and low-dose PET images for its training process, where the normal-dose JCP serves as a guiding parameter to enhance the transformer's learning performance. Initially, the normal-dose PET and low-dose PET are downsampled using the PixelUnshuffle operation to serve as the input for the JCP extraction block. The low-dose JCP is utilized to reconstruct the corresponding normal-dose JCP in the reconstruction phase. Subsequently, normal-dose JCP is then extracted by the

JCP extraction block, denoted as J. As illustrated in Fig. 3, JCP is then utilized as dynamic modulation parameters in the multi-head transposed attention and gated feed-forward network of the transformer stage to guide PET training:

$$A^{'} = W_l^1 J \odot \mathrm{Norm}(A) + W_l^2 J \tag{3}$$

where $\odot$ indicates element-wise multiplication, Norm denotes layer normalization, W_l represents linear layer, A and $A^{'}$ are input and output feature maps respectively.

In the multi-head transposed attention, global spatial information is aggregated by projecting $A^{'}$ into query $Q = W_d^Q W_c^Q A^{'}$, key $K = W_d^K W_c^K A^{'}$, and value $V = W_d^V W_c^V A^{'}$ matrices, followed by reshaping and dot-product operations to generate a transposed-attention map. This map is further processed using learnable scaling parameter γ and channel separation to generate attention map:

$$\widehat{A} = W_c \widehat{V} \cdot \mathrm{Softmax}(\widehat{K} \cdot \widehat{Q} / \gamma) + A \tag{4}$$

where Softmax is an activation function that converts a vector of values into a probability distribution, where each value's probability is proportional to the exponential of the input value, typically used in the output layer of a classification neural network [18]. The gated feed-forward network aggregates local features by employing 1×1 Conv layers to aggregate information from different channels and 3×3 depth-wise Conv layers to aggregate information from spatially neighboring pixels. Additionally, the gating mechanism is applied to enhance information encoding. The gated feed-forward network is characterized by the following process:

$$\widehat{A} = \mathrm{GELU}(W_d^1 W_c^1 A^{'}) \odot W_d^2 W_c^2 A^{'} + A \tag{5}$$

where GELU, Gaussian error linear unit, is an activation function that uses a smooth, non-linear transformation based on the Gaussian cumulative distribution function to activate neurons in a neural network [38]. The JCP extraction block and transformer stage are jointly trained, enabling the transformer stage to effectively utilize JCP for PET reconstruction.

In the diffusion stage, JCP is trained using the strong data estimation ability of the diffusion stage. The JCP extraction block is utilized to capture J, which is then subjected to the diffusion process to sample J_T:

$$q(J_T | J) = \mathcal{N}(J_T; \sqrt{\overline{\alpha}_T} J, (1 - \overline{\alpha}_T) x) \tag{6}$$

$$\alpha_T = 1 - \beta_t; \overline{\alpha}_T = \Pi_{i=0}^{t} \alpha_i \tag{7}$$

where T is the total number of iterations, β_t indicates the predefined scale factor.

In summary, DTM has two training stages: the transformer stage and the diffusion stage. In the transformer stage, DTM directly uses the JCP of the normal-dose PET to guide the training of the transformer, focusing on the complete PET data. In the diffusion stage, only the JCP is trained separately without the need to train the whole PET images.

3.3. Reconstruction Procedure

During the reconstruction procedure in Fig. 4, a lesion based DCS is proposed to reconstruct low-dose PET images. It is composed of a lesion refining block combined with the ADMM algorithm. Meanwhile, the JCP-based diffusion stage and transformer stage are also utilized in this procedure.

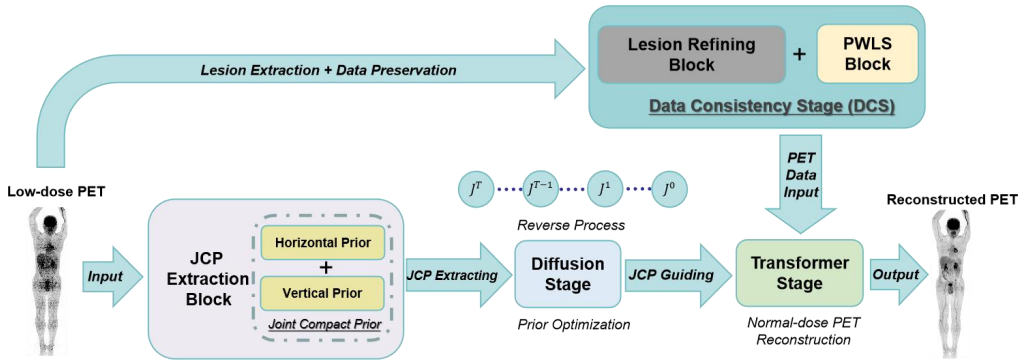

Fig. 4. The pipeline of DTM reconstruction procedure. A data consistency stage is involved to inference procedure for lesion refining and detail preserving. JCP of low-dose PET will be reconstructed to JCP of normal-dose PET through diffusion stage. Normal-dose PET will be reconstructed from low-dose PET through JCP guiding and detail preserving by DCS.

DTM initiates from the T -th time step and conducts all denoising iterations to derive $\hat{J}$, which is subsequently forwarded to the transformer stage for joint optimization:

$$\hat{J}_{t-1} = \frac{1}{\sqrt{\alpha_t}} \left(\hat{J}_t - \epsilon \frac{1 - \alpha_t}{\sqrt{1 - \overline{\alpha}_t}} \right) \tag{8}$$

where symbol ϵ represents the same noise, for which we employ the JCP extraction block and denoising process to make predictions. Notably, in contrast to traditional diffusion models, our DTM eliminates variance estimation, which is beneficial for accurate JCP estimation and improved performance.

During the reverse process of the diffusion stage, we initially utilize the JCP extraction block to derive a conditional vector J from the low-dose PET. Subsequently, the denoising process is utilized to estimate noise at each time step, denoted as ϵ_t. This

estimated noise is then incorporated into Eq. (8) to obtain $\hat{J}_{t-1}$, which serves as the starting point for the subsequent iteration. Following T iterations, we arrive at the final estimated JCP $\hat{J}$. Subsequently, the transformer module leverages the JCP for the reconstruction of low-dose PET data.

In DCS, we introduce an innovative lesion refining block that automatically extracts lesions from low-dose PET data x^0 by identifying high-value regions, which corresponds to areas where the tracer accumulates. Subsequently, target reconstruction x^i is generated, specifically tailored to these lesion refining data u^i. By integrating lesion refining block with the ADMM algorithm, we significantly enhance the recovery capability of lesion regions, achieving a positive stride for lesion recovery. The overall optimization equation of DTM can be expressed as follows:

$$\begin{aligned} x^{i+1} &= \underset{x}{\operatorname{argmin}}[\|y-\zeta(u^i)\|^2+\mu R(x^i,\hat{J})] \\ s.t. \quad & M\odot x^i = v^i \\ & u^i = [(x^i+\eta v^i)/2] \end{aligned} \tag{9}$$

where low-dose PET data x^0 is used as input for the reconstruction process to approximate normal-dose data y. The operator ζ is applied for reconstructing the normal-dose PET and i refers to the ADMM iteration number. The regularization term $R(x^i,\hat{J})$ incorporates JCP information to constrain the solution. Moreover, a high-value region v^i is extracted for refining lesion information. To create the binary mask M, we extract the maximum 2% of pixel values from the input low-dose PET data and set to 1 for the identified high-value regions and 0 elsewhere. μ and η are modulating factors to maintain the consistency of DTM. The value of x^{i+1} is determined by x^i, u^i and v^i during the iterative solving process.

The ADMM formulation can be defined as follows:

$$L(x,u,\lambda_1,\lambda_2)=\|y-\zeta(u^i)\|^2+\lambda_1(M\odot x^i-v^i)+\lambda_2\left(u^i-\frac{x^i+\eta v^i}{2}\right)+\frac{\rho}{2}\|M\odot x^i-v^i\|^2+\frac{\gamma}{2}\left\|u^i-\frac{x^i+\eta v^i}{2}\right\|^2+\mu R(x^i,\hat{J}) \tag{10}$$

where λ_1 and λ_2 are Lagrange multipliers. ρ and γ are penalty parameters used to control the strength of the penalty imposed by the constraint conditions. Eq. (10) can be broken into two subproblems by updating the variables iteratively:

Subproblem 1 ← Update x^{i+1} by minimizing:

$$x^{i+1}=\underset{x}{\operatorname{argmin}}[\lambda_1(M\odot x^i-v^i)+\lambda_2\left(u^i-\frac{x^i+\eta v^i}{2}\right)+\frac{\rho}{2}\|M\odot x^i-v^i\|^2+\frac{\gamma}{2}\|u^i-\frac{x^i+\eta v^i}{2}\|^2+\mu R(x^i,\hat{J})] \tag{11}$$

Subproblem 2 ← Update u^{i+1} by minimizing:

$$u^{i+1}=\underset{u}{\operatorname{argmin}}\,[\|y-\zeta(u^i)\|^2+\lambda_2\left(u^i-\frac{x^i+\eta v^i}{2}\right)+\frac{\gamma}{2}\|u^i-\frac{x^i+\eta v^i}{2}\|^2] \tag{12}$$

Algorithm 1 offers a detailed description of low-dose PET reconstruction, where δ represents the learning rate, and κ represents the convergence threshold.

Algorithm 1: DTM for Reconstruction

Require: $x^0, v^0, u^0, i, \zeta, \hat{J}, M, \eta$
1: Initialization: x^0, v^0, and u^0
2: For $i = 0$ to 2 do
3: **Update** x^{i+1} via Eq. (11)
4: **Update** u^{i+1} via Eq. (12)
5: Take a gradient descent step on $\nabla_x L$
$x^{i+1} \leftarrow x^i - \delta\nabla_x L$
6: **If** $\|x^{i+1}-x^i\| < \kappa$
7: **Else** $i \leftarrow i+1$
8: **End if**
9: End for
10: Return x^{i+1}

3.4. Distinctive Characteristics

We introduce a JCP to guide PET reconstruction through DTM. In the diffusion stage, the compact structure of JCP enables DTM to achieve robust estimations with fewer iterations and smaller model size compared to traditional diffusion models. Traditional diffusion models incur substantial computational costs during iterations, necessitating the random sampling of time steps for denoising optimization. Moreover, the lack of joint training between the denoising process and the decoder means that minor estimation errors from the denoising process can hinder the transformer's full potential. As represented in Eq. (9), JCP is incorporated into the regularization term, enhancing the reconstruction procedure.

Beyond JCP, we also introduce the innovative lesion refining block. This block systematically evaluates all data points from the input PET data, identifying areas that closely resemble lesions. These identified regions are reintroduced into DTM for reconstruction. The reconstructed results are then merged back into the transformer stage using weighting mechanisms to achieve an optimal PET reconstruction outcome. This method addresses a common challenge in many deep learning models, where noise removal may inadvertently lead to the loss of lesion areas. The lesion refining block effectively mitigates this issue by specifically targeting and preserving lesion information during the denoising process, ensuring more accurate and comprehensive recovery of

relevant anatomical features in PET images. The functions of lesion refining block can be expressed as the constraint conditions, detailed in Eq. (9). By introducing these constraint conditions, the search space for solutions is minimized, ensuring an optimal solution within the specific constraints. The penalty terms $\frac{\rho}{2}\|M \odot x^i - v^i\|^2$ and $\frac{\gamma}{2}\|u^i - (x^i + \eta v^i)/2\|^2$ can make the optimization problem more proximate to the actual optimal solution.

In summary, our distinctive characteristics include the integration of JCP for guided PET reconstruction and the lesion refining block with ADMM algorithm for preserving critical lesion and detailed structure information. These advancements significantly improve the robustness and accuracy of low-dose PET imaging, offering a more reliable tool for clinical diagnosis and early disease detection.

4. Experiments

In this section, we introduce the implementation details of the proposed DTM, as well as the datasets we used for evaluation. Subsequently, the reconstruction results are reported and analyzed. Both quantitative and qualitative evaluations are comprehensively conducted to investigate the performance of DTM. Patient data is used for training and ablation studies, while phantom data is employed for generalization experiments.

4.1. Data Specification

The experiment data is generated by the DigitMI 930 PET/CT scanner. This scanner is developed by RAYSOLUTION Healthcare Co., Ltd, and incorporate state-of-the-art all-digital PET detectors. The PET scanner has an axial field-of-view (AFOV) of 30.6 cm within an 81 cm ring diameter.

Patient data: A comprehensive data set is utilized, consisting of 19 patients. Each patient undergoes a scan ranging from 4 to 8 beds, with a complete sampling scan time of 45 seconds to 3 minutes per bed. The low-dose PET is performed through resampling at regular intervals. Specifically, the listmode data is segmented based on the chronological sequence, with each cycle representing a 2 millisecond (ms) interval. During each cycle, data within a 1 ms interval is retained, while the remaining data is discarded. Finally, the low-count data is rearranged into image domain. The training data comprises a total of horizontal 25986 2D slices with dimensions of 256×256 and vertical 45384 2D slices with dimensions of 256×144 normal-dose PET data from 12 patients, while the test data is obtained from half dose, quarter dose, and one-tenth dose PET voxels from 7 patients. This study is approved by the institutional review board of the Beijing Friendship Hospital, Capital Medical University, Beijing, China. The approval number is 2022-P2-314-01.

Phantom data: To assess image quality using body phantom data, a NEMA body phantom with an interior length of 180 millimeter (mm) was utilized. This phantom contained six fillable spheres with internal diameters of 10 mm, 13 mm, 17 mm, 22 mm, 28 mm, and 37 mm. It was filled with 18F-FDG, having a background activity concentration of 5.3 kBq/ml. The activity concentration in the fillable spheres was four times that of the background.

4.2. Model Training and Parameter Selection

In the experiments, DTM is implemented in Python and PyTorch on a personal workstation with a GPU card (NVIDIA RTX-3090-24GB). The proposed approach employs a 4-level encoder-decoder structure. Within the transformer stage, the multi-head transposed attention mechanism utilizes attention heads with configurations of [1, 2, 4, 8], accompanied by respective channel numbers of [48, 96, 192, 384]. Specifically, across levels 1 to 4, the number of dynamic transformer blocks is configured as [3, 5, 6, 6]. Additionally, the number of channels for the JCP extraction block is set to 64. In the diffusion stage, T is set to 4. Adam optimizer is set to $\beta_1 = 0.9$ and $\beta_2 = 0.99$. For ADMM algorithm, i is set to 2. The open-source code is available at: https://github.com/yqx7150/DTM.

4.3. Quantitative Indices

To evaluate the quality of the reconstructed data, peak signal-to-noise ratio (PSNR), structural similarity index (SSIM), normalized root mean squared error (NRMSE), contrast ratio (CR) and coefficient of variation (COV) are used for quantitative assessment.

PSNR describes the maximum possible power of the signal in relation to the noise corrupting power. Higher PSNR means better image quality. Denoting x and y to be the estimated reconstruction and the reference image, PSNR is expressed as:

$$PSNR(x, y) = 20\log_{10}[\,Max(y)/\|x-y\|_2\,] \tag{13}$$

SSIM is used to measure the similarity between the ground-truth and reconstruction, and it is defined as:

$$SSIM(x, y) = \frac{(2\mu_x\mu_y+c_1)(2\sigma_{xy}+c_2)}{(\mu_x^2+\mu_y^2+c_1)(\sigma_x^2+\sigma_y^2+c_2)} \tag{14}$$

where μ_x and σ_x^2 are the average and variances of x. σ_{xy} is the covariance of x and y. c_1 and c_2 are used to maintain a stable constant. NRMSE is employed to evaluate the errors and it is defined as:

$$NRMSE(x, y) = \sqrt{\sum_{i=1}^{W}\|x_i-y_i\|_2/W}/(\bar{y}_{mean}) \tag{15}$$

where W is the number of pixels within the reconstruction result. If NRMSE approaches to zero, the reconstructed image is closer to the reference image.

The calculation of CR involves comparing the maximum pixel value M_{lesion} within the lesion region of the patient to the mean pixel value μ_{liver} in the liver region:

$$CR = M_{lesion}/\mu_{liver} \tag{16}$$

COV quantifies the variation in signal intensity across a selected region, like liver, of the reconstructed data. It is computed as the ratio of the standard deviation σ_{liver} to the mean μ_{liver} of the pixel values, providing insights into the uniformity of the reconstructed image:

$$COV = \sigma_{liver}/\mu_{liver} \tag{17}$$

By incorporating CR and COV alongside PSNR, SSIM, and NRMSE, a more comprehensive evaluation of the reconstructed data's quality is achieved, encompassing aspects of contrast, noise, and uniformity.

4.4. Experimental Comparison

The proposed DTM is compared with six baseline models for low-dose PET reconstruction: Denoise [14], NLM [13], DDPM [24], Restomer [39], NCSN++ [40], and Pix2pix-3D [41]. Among these, DDPM is an unsupervised diffusion model designed to generate high-quality images, while Restomer is a supervised Transformer-based model for image restoration. Similarly, NCSN++ is an unsupervised score-based diffusion model that generates clear images, and Pix2pix-3D is a supervised 3D-GAN aimed at denoising low-dose medical images. The involved parameters for each baseline are set according to the guidelines provided in their original papers.

In this section, half-dose, quarter-dose, and one-tenth-dose PET images are utilized as input during the inference phase, with normal-dose PET images serving as the ground truth. The PSNR, SSIM, and NRMSE values of the reconstructed results from the DigitMI 930 PET/CT scanner are listed in Table I, with the best values highlighted in bold. Among the baseline models, DDPM performs poorly under lower dose conditions, particularly in terms of SSIM, which highlights its limited 3D reconstruction capability. This is evident from noticeable data discontinuities in the reconstructed images. In contrast, Restormer, a supervised 2D network, exhibits superior denoising performance compared to DDPM, achieving an impressive average PSNR of 55.88 dB and an NRMSE of 1.022 for half-dose PET. However, it compromises the recovery of tracer uptake regions, leading to suboptimal preservation of critical features. Meanwhile, Pix2pix-3D demonstrates a balanced performance in both denoising and structural preservation, achieving results that rank among the best for baseline models. In general, DTM presents more details and less noise compared to all other methods. It achieves the best average NRMSE value of 0.83 for half-dose PET images reconstructed for 7 patients, highlighting its ability to suppress noise effectively. Furthermore, DTM reaches an impressive 47.81 dB PSNR in the case of one-tenth-dose PET, with reconstructed images containing fewer artifacts and more preserved details. In terms of SSIM, DTM consistently outperforms the other methods, showcasing visible gains in noise and artifact suppression, and making it the most robust method for low-dose PET reconstruction.

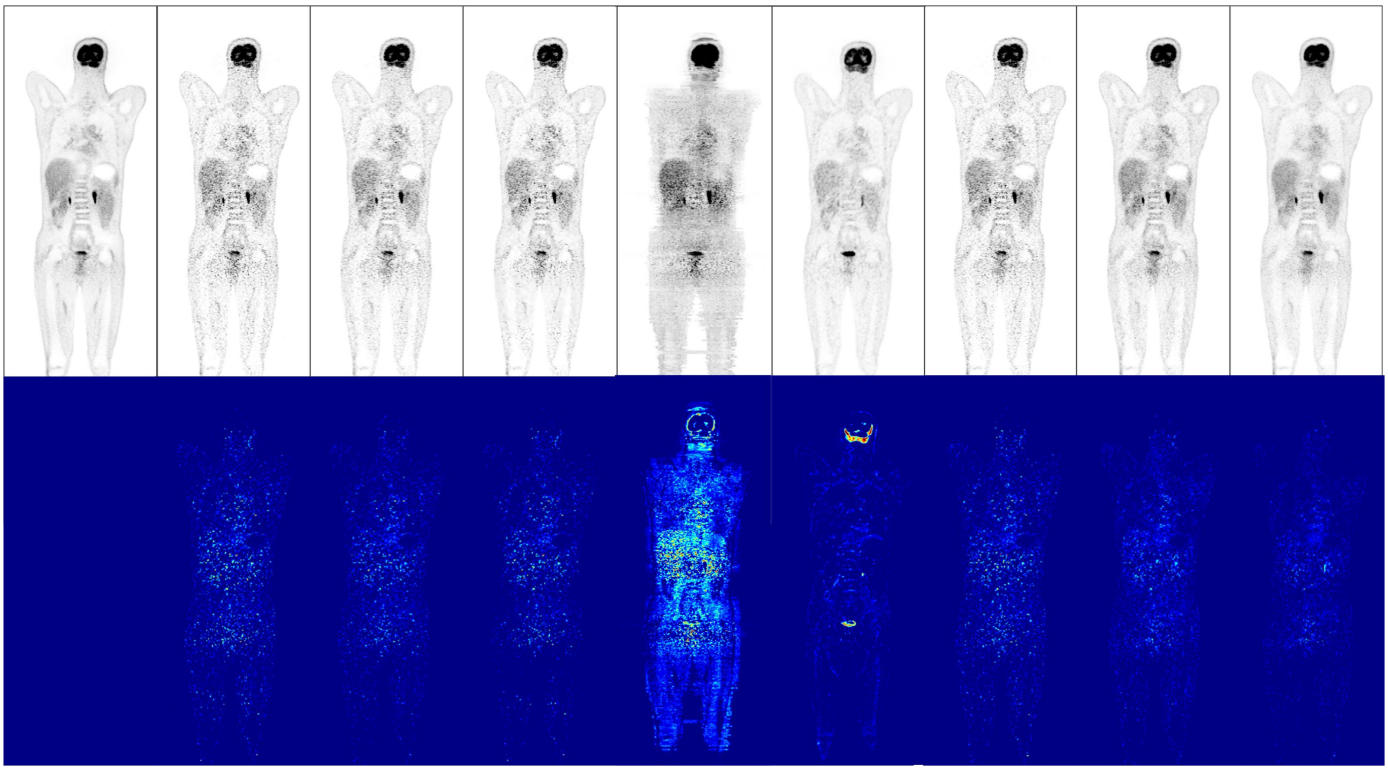

(a) Reference (b) 10% dose PET (c) Denoise (d) NLM (e) DDPM (f) Restomer (g) NCSN++ (h) Pix2pix-3D (i) DTM

Fig. 5. Reconstruction results for coronal images using different methods. (a) The normal-dose PET and (b) 10% dose image versus the images reconstructed by (c)

Denoise, (d) NLM, (e) DDPM, (f) Restomer, (g) NCSN++, (h) Pix2pix-3D, and (i) DTM. The second row depicts the residuals between the reference and reconstructed images.

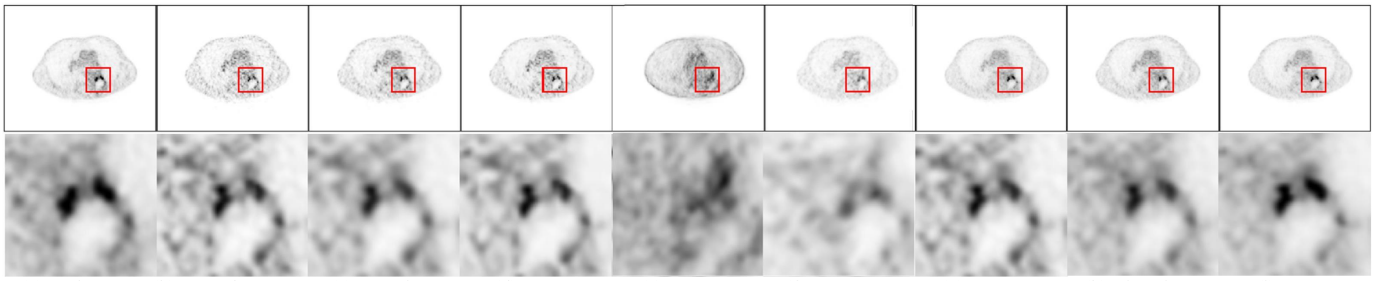

(a) Reference (b) 10% dose PET (c) Denoise (d) NLM (e) DDPM (f) Restomer (g) NCSN++ (h) Pix2pix-3D (i) DTM

Fig. 6. Reconstruction results for transverse images using different methods. (a) The normal-dose PET and (b) 10% dose image versus the images reconstructed by (c) Denoise, (d) NLM, (e) DDPM, (f) Restomer, (g) NCSN++, (h) Pix2pix-3D, and (i) DTM. The second row depicts the magnified detail images.

TABLE I
RECONSTRUCTION PSNR/SSIM/NRMSE FROM DIGITMI 930 PET/CT SCANNER USING DIFFERENT METHODS AT 50%, 25% AND 10% DOSE.

PET Dose	Denoise	NLM	DDPM	Restomer	NCSN++	Pix2pix-3D	DTM
50%	55.18/0.8232/1.133	55.84/0.8598/1.067	55.01/0.6183/1.129	55.88/0.8713/1.022	55.90/0.8757/1.044	56.44/0.8982/0.907	**56.70/0.9011/0.830**
25%	51.12/0.8194/1.487	50.94/0.8354/1.763	51.77/0.5351/1.508	50.83/0.8086/1.676	51.02/0.8117/1.647	52.07/0.8698/1.187	**52.54/0.8819/1.067**
10%	45.54/0.7879/2.276	45.17/0.8210/2.994	44.78/0.3730/5.241	45.12/0.7732/2.776	45.68/0.7846/2.490	46.75/0.8457/1.666	**47.81/0.8743/1.349**

To further illustrate the merits of DTM, the reconstructed images and residual images at 10% dose are depicted in Figs. 5-6. The Fig. 6 displays magnified images concerning the transverse graphs, while Fig. 5 presents residual maps for the coronal graphs. As depicted in Figs. 5-6, the Denoise method produces the poorest results due to the excessive blurring of lesions during the denoising process. While Pix2pix-3D showcases commendable denoising capabilities, its ability to reconstruct lesions is inadequate. The residual maps generated by DDPM perform the worst, as it fails entirely to recover the shape of lesion regions. On the other hand, Restormer over-smooths the images during the denoising process, leading to the loss of critical structural details. In contrast, images reconstructed by DTM closely approximate the ground truth, displaying preserved lesions and minimal noise levels.

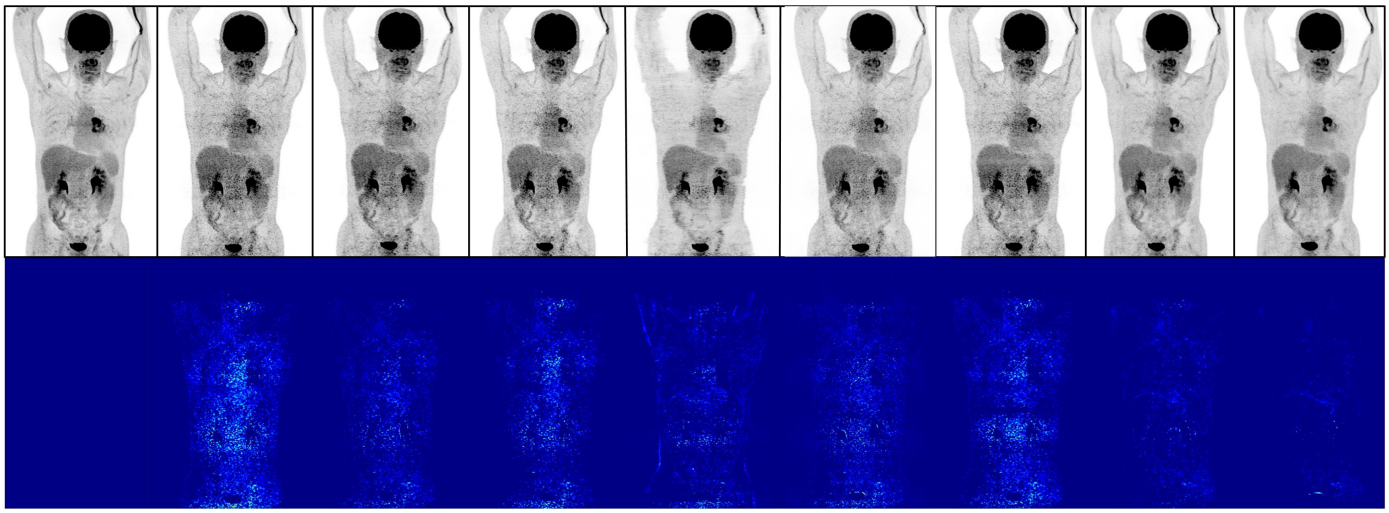

(a) Reference (b) 25% dose PET (c) Denoise (d) NLM (e) DDPM (f) Restomer (g) NCSN++ (h) Pix2pix-3D (i) DTM

Fig. 7. Reconstruction results for MIP images using different methods. (a) The normal-dose PET and (b) 25% dose image versus the images reconstructed by (c) Denoise, (d) NLM, (e) DDPM, (f) Restomer, (g) NCSN++, (h) Pix2pix-3D, and (i) DTM. The second row depicts the residuals between the reference and reconstructed images.

In the context of coronal maximum intensity projection (MIP) images at 25% dose are depicted in Fig. 7. As NCSN++ is a 2D unsupervised model, it introduces horizontal streak artifacts when reconstructing 3D MIP images. This limitation significantly affects its performance, leading to the poorest results among the compared algorithms in terms of residual maps.

Conversely, images reconstructed by NLM and Denoise methods exhibit limited denoising capabilities. Increasing denoising parameters would lead to over-smoothing of images, consequently reducing lesion contrast. Under relatively higher dose conditions, DDPM demonstrates a significant improvement in denoising performance. However, its ability to preserve structural details remains poor. In contrast, Restomer shows a noticeable enhancement in lesion contrast preservation compared to the 10% dose case, albeit with a slight decline in its overall denoising performance. Additionally, the Pix2pix-3D method performs moderately well in discerning certain details, ranking second in effectiveness. In contrast, images reconstructed by DTM excel in preserving a broader array of structural details while effectively mitigating streaking artifacts, thereby demonstrating superior

performance. These results are consistent with the values presented in Table II.

TABLE II
RECONSTRUCTION CR/COV FROM DIGITMI 930 PET/CT SCANNER USING DIFFERENT METHODS AT 25% DOSE.

Lesion ID	Normal-dose PET	Low-dose PET	Denoise	NLM	DDPM	Restomer	NCSN++	Pix2pix-3D	DTM
1	2.221/0.196	2.026/0.294	2.013/0.243	2.036/0.255	1.953/0.177	2.486/0.249	2.006/0.224	1.924/0.181	**2.366/0.168**
2	2.745/0.293	2.727/0.542	2.210/0.449	2.288/0.280	2.962/0.434	2.603/0.362	2.569/0.407	2.465/0.307	**2.578/0.280**
3	3.095/0.236	4.155/0.483	3.656/0.395	4.006/0.442	3.944/0.406	3.473/0.392	3.974/0.271	3.359/0.246	**3.318/0.211**
4	3.342/0.224	3.382/0.463	3.044/0.379	3.575/0.425	3.972/0.417	3.545/0.413	3.643/0.255	2.4545/0.229	**3.509/0.197**

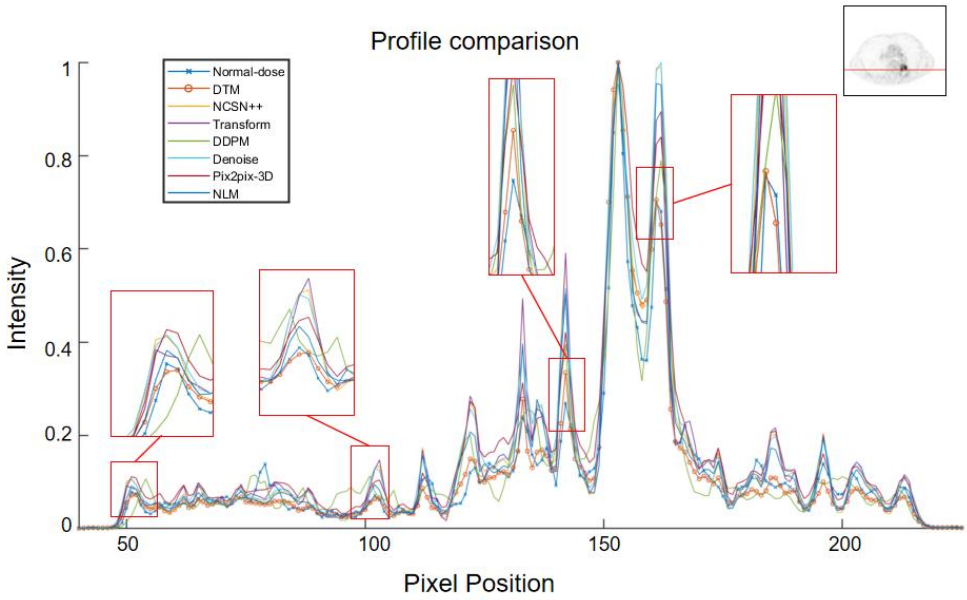

Fig. 8. Comparison of PET image profiles between the reference and other four methods on lesion area at 25% dose.

Moreover, CR evaluation is performed on 3D regions within five lesion sites across different patients in Table II. The calculation of CR involves comparing the maximum pixel value within the lesion region of the patient to the mean pixel value in the liver region. Remarkably, the CR value of DTM is the closest to that of normal-dose PET compared to the other four methods. A CR value closer to that of normal-dose PET indicates better contrast recovery for lesions. The COV values are calculated in the liver regions. A smaller COV value indicates lower dispersion of image pixel values, meaning that the grayscale or color values are more spatially consistent. This is particularly important in medical image processing and quality control, as a lower COV typically signifies higher image quality and lower noise level.

For evaluating the edge-preserving performances, the profile lines for the reconstructed results of different methods are compared in this section. In Fig. 8, a profile line was drawn through the lesion area of a patient, revealing two peak values. The profiles generated by Denoise, NLM, NCSN++, and Pix2pix-3D perform adequately at the first peak value but fail to recover the second peak. DDPM shows a considerable improvement in recovering the second peak compared to these methods, with a slightly smoother profile around the edges. Restomer also performs notably well, achieving enhanced profile preservation at the second peak, though it introduces minor deviations near the baseline intensities. In contrast, DTM closely matches the ground truth at both peaks, demonstrating the strong profile-preserving capability of the diffusion model. In comprehensive comparison, DTM generates the most accurate profile.

4.5. Ablation Study

Through the ablation study, a better understanding of the impact of each component on DTM's performance, as well as their role within the entire model, can be attained. JCP and DCS within DTM will be analyzed. JCP includes vertical and horizontal compact priors, while DCS includes the lesion refining block and ADMM block.

TABLE III
RECONSTRUCTION CR/COV USING DIFFERENT METHODS AT 25% DOSE.

Lesion ID	(w/o) JCP&DCS	(w/o) DCS	(w/o) JCP	DTM	Normal-dose PET
1	1.969/0.182	1.898/**0.136**	2.567/0.205	**2.366**/0.168	2.221/0.196
2	2.054/0.236	1.924/**0.184**	**2.775**/0.354	2.578/0.280	2.745/0.293
3	3.126/0.124	2.499/**0.087**	3.451/0.401	**3.318**/0.211	3.095/0.236

4	2.166/0.112	1.899/**0.075**	3.580/0.384	**3.509**/0.197	3.342/0.224

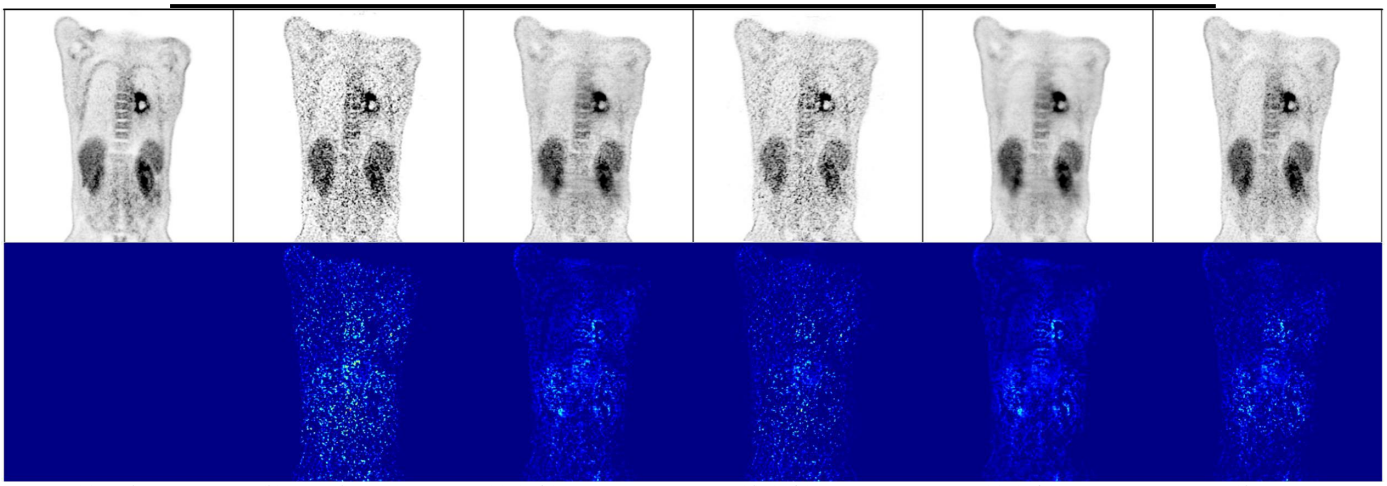

(a) Reference (b) 10% dose PET (c) (w/o) JCP&DCS (d) (w/o) JCP (e) (w/o) DCS (f) DTM

Fig. 9. Reconstruction results for coronal images using different methods. (a) The normal-dose PET and (b) 10% dose image versus the images reconstructed by (c) (w/o) JCP&DCS, (d) (w/o) JCP, (e) (w/o) DCS and, (f) DTM. The second row depicts the residuals between the reference and reconstructed images.

Based on Fig. 9 and Table III, it can be observed that JCP further enhances the model's denoising capability, achieving the lowest COV values. However, this improvement comes at the cost of over-smoothing, which can degrade important image details. The results of the model without JCP (w/o JCP) show that excluding JCP leads to a decline in denoising performance. Introducing DCS enhances lesion recovery capability but also introduces additional noise, which becomes increasingly pronounced as the dose decreases, especially at 10% dose, as indicated by higher COV values compared to the full model. Consequently, the combination of w/o JCP & DCS demonstrates only moderate denoising and reconstruction capabilities. However, using DCS without JCP causes the model to become imbalanced, leading to reconstructed images with excessive noise that cannot be effectively removed. In contrast, using JCP without DCS results in overly smooth images, further compromising structural detail preservation. At last, simultaneously applying JCP and DCS can achieve a balance between noise reduction and detail preservation. This combination results in better lesion recovery and lower noise level.

4.6. Generalization and Robustness Analysis

Phantom Reconstruction Results: To further validate the robustness of our proposed learning scheme, we change the test data to phantom data and evaluate its generalization performance. The results obtained on the phantom data are presented in Table IV. Impressively, DTM achieves the highest quantitative indices when compared with other comparison methods. In the experiments assessing generalization, the model was not retrained, and the original training model was utilized. This may explain the decline in reconstruction performance of Restomer, Pix2pix-3D and NCSN++, particularly for Restomer. DDPM achieves a PSNR of 36.79 dB. But it falls short in terms of SSIM, indicating its potential limitation in structural preservation for phantom data. Restomer shows moderate results with a PSNR of 34.95 dB and an SSIM close to Denoise, showcasing its consistency across datasets but with slightly higher NRMSE. On the other hand, Denoise and NLM demonstrate relatively stable results, with slight fluctuations in the quantitative indices. Conversely, traditional algorithms such as Denoise and NLM can process various datasets because they do not require training. However, the reconstructed result of DTM is 40.49 dB higher than Denoise and NLM respectively. Our DTM outperforms Denoise, NLM, NCSN++, Pix2pix-3D, DDPM, and Restomer with higher performance and stronger generalization capability.

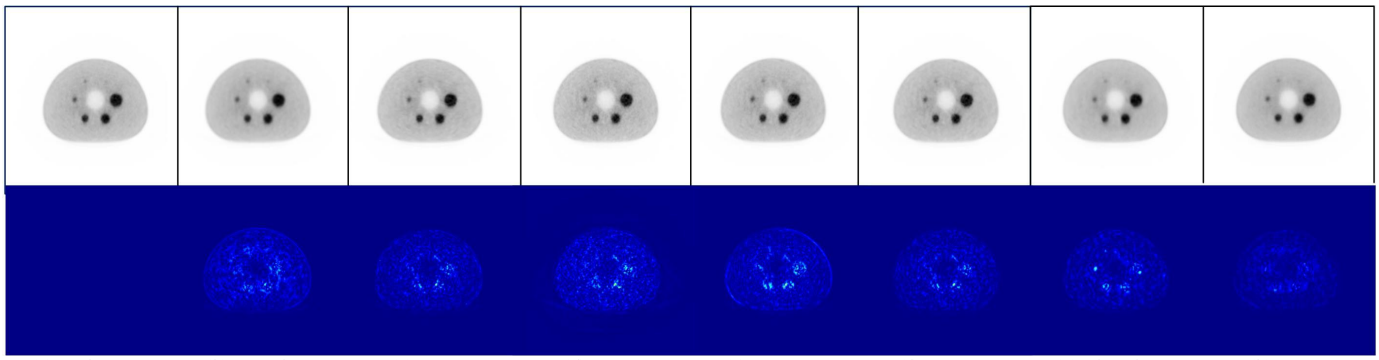

(a) Reference (b) Denoise (c) NLM (d) DDPM (e) Restomer (f) NCSN++ (g) Pix2pix-3D (h) DTM

Fig. 10. Reconstruction results for phantom data at 50% dose using different methods. (a) The normal-dose PET versus the images reconstructed by (b) Denoise, (c) NLM, (d) DDPM, (e) Restomer, (f) NCSN++, (g) Pix2pix-3D, and (h) DTM. The second row depicts the residuals between the reference and reconstructed images.

TABLE IV
RECONSTRUCTION PSNR/SSIM/NRMSE FOR PHANTOM DATA AT 50% DOSE.

Methods	PSNR	SSIM	NRMSE
Denoise	35.28	0.7461	0.133
NLM	35.04	0.6882	0.136
DDPM	36.79	0.3717	0.125
Restomer	34.95	0.7478	0.143
NCSN++	32.56	0.7560	0.131
Pix2pix-3D	34.79	0.7158	0.138
DTM	**40.49**	**0.8116**	**0.065**

In Fig. 10, the visual effects of DTM are also exceptional. Pix2pix-3D demonstrates some ability to suppress noises but loses the ability to reconstruct radiated areas. For NCSN++, subtle artifacts and blurred internal structures still persist. In comparison to NCSN++ and NLM, the result of the Denoise shows a slight inferiority. NCSN++ producing smoother results than DDPM while maintaining better details in radiated areas. However, minor residual noise is still noticeable. Restomer, on the other hand, exhibit slightly higher noise levels in uniform areas compared to other methods. In contrast, the DTM approach demonstrates excellent reconstruction capability and effectively compensates for the artifacts in low-dose PET using phantom data. When compared to other competitive reconstruction methods, DTM excels in terms of noise-artifact reduction and detail preservation, offering the best visual results.

5. Discussion

Proposed DTM demonstrates outstanding performance and versatility in various PET imaging tasks. This section will present and analyze the results of normal-dose PET denoising and ultra-low-dose PET reconstruction

Normal-dose PET Denoising: Our DTM not only has the capability to restore or reconstruct low-dose PET into normal-dose PET, but also aids in processing normal-dose PET denoising. In Fig. 11, we display zoomed mediastinal position marked by red rectangles. In comparison to normal-dose PET, the outcomes produced by DTM exhibit greater clarity with lower COV calculated in different areas.

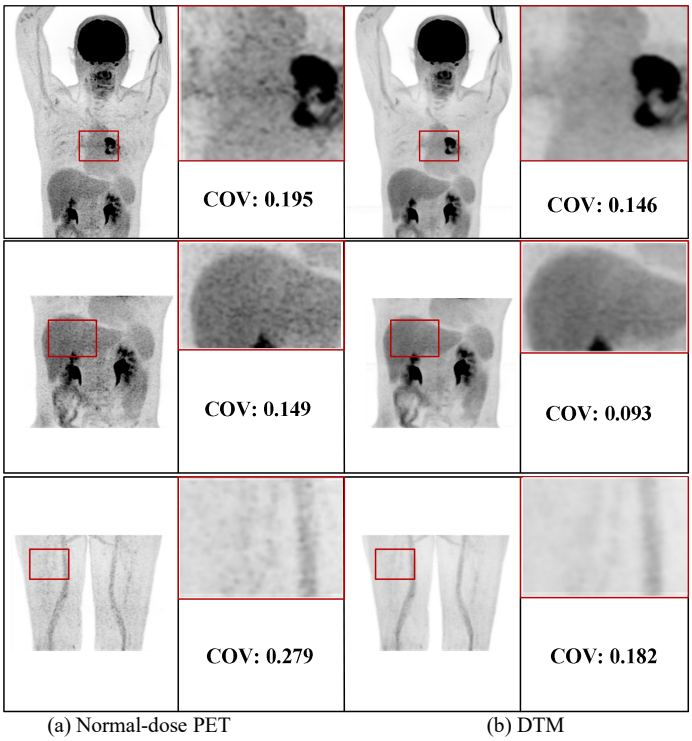

(a) Normal-dose PET (b) DTM

Fig. 11. Reconstruction results for MIP images using DTM at normal-dose PET. (a) The normal-dose PET versus the image reconstructed by (b) DTM.

Ultra-low-dose PET Reconstruction: When it comes to ultra-low-dose PET reconstruction, DTM can still achieve remarkable results. Without retraining using ultra-low-dose PET, we use DTM to reconstruct from 1% dose PET data. The reconstruction results in Fig. 12 exhibit minimal noise and closely approximate the normal-dose PET, demonstrating the DTM's robust reconstruction capabilities and strong generalization ability.

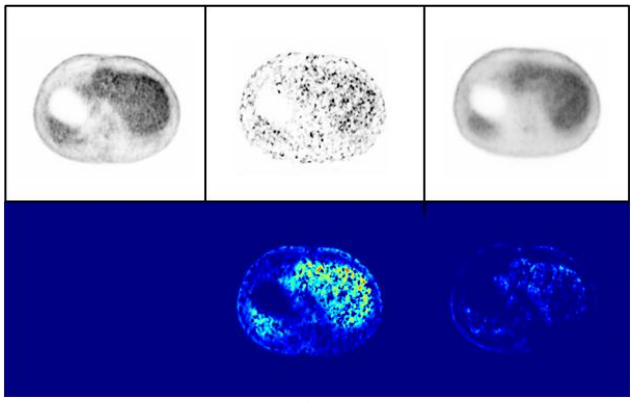

(a) Reference (b) 1% dose PET (C) DTM

Fig. 12. Reconstruction results for transverse images using DTM at 1%-dose PET. (a) The normal-dose PET and (b) 1% dose image versus the image reconstructed by (c) DTM. The second row depicts the residuals between the reference and reconstructed images.

The conducted experiments demonstrate that DTM can serve as a multitask model, capable of denoising normal-dose PET and reconstructing low-dose and ultra-low-dose PET. This showcases its exceptional task adaptability and reconstruction capabilities. The model's versatility allows it to perform excellently across various PET imaging tasks at different dose levels. With further improvements and exploration of DTM, we anticipate uncovering additional applications and potential in PET imaging.

6. Conclusions

Although deep learning-based PET reconstruction methods have achieved significant success in recent years, ensuring high predictive accuracy and robustness of the trained networks remained a challenging issue. In this study, we introduced a novel diffusion transformer approach for low-dose PET reconstruction. Our approach leveraged JCP extraction block to capture the joint prior distribution of normal-dose PET data. Lesion refining block and ADMM were utilized together to preserve the lesion information and detailed structures. Experimental results underscored the effectiveness of the DTM in suppressing the well-known streaking artifacts and preserving crucial image details. These findings positioned DTM as a robust and reliable solution for the challenges associated with low-dose PET reconstruction. Moreover, DTM can serve as a multitask model, capable of denoising normal-dose PET and reconstructing low-dose and ultra-low-dose PET. This study demonstrated that combining the diffusion and transformer models can enhance reconstruction performance and detail richness. Future research endeavors can explore the application of deep learning in real-time PET image reconstruction.

Data availability statement

The data cannot be made publicly available upon publication because no suitable repository exists for hosting data in this field of study. The data that support the findings of this study are available upon reasonable request from the authors.

Acknowledgments

This research was supported in part by National Key Research and Development Program of China under the Reference Number 2024YFC2419800, in part by National Natural Science Foundation of China under the Reference Number 62122033 and 62201193, in part by Nanchang University Interdisciplinary Innovation Fund Project under the Reference Number PYJX20230002, and in part by Open Fund of Anhui Province Key Laboratory of Biomedical Imaging and Intelligent Processing under the Reference Number 23YGXT002 and 24YGXT004.

Ethical Statement

The research was conducted under the oversight of the Ethics Committee at Beijing Friendship Hospital, Capital Medical University (IRB), with the approval number 2022-P2-314-01. The Ethics Committee has approved this study following relevant regulations and ethical principles, and informed consent from the human subjects involved in the research has been obtained.

References

[1] M. E. Phelps, “Positron emission tomography provides molecular imaging of biological processes,” *PNAS.* vol. 97, no. 16, pp. 9226-9233, 2000.

[2] R. S. Cherry, “Fundamentals of positron emission tomography and applications in preclinical drug development,” *J. Clin. Pharmacol*, vol. 41, no. 5, pp. 482-491. 2001.

[3] A. M. Alessio, P. E. Kinahan, M. Vivek, G. Victor, A. Lisa, and M. T. Parisi, “Weight-based, low-dose pediatric whole-body PET/CT protocols,” *J. Nucl. Med*, vol. 50, no. 10, pp. 1570-1578, 2009.

[4] W. D. Townsend, "Multimodality imaging of structure and function," *Phys. Med. Biol*, vol. 53, no. 4, pp. R1, 2008.

[5] J. D. Brenner, and E. J. Hall, "Computed tomography—an increasing source of radiation exposure," *New Eng. J. Med*, vol. 357, no. 22, pp. 2277-2284, 2007.

[6] H. Kirpalani, and N. Claude, "Radiation risk to children from computed tomography," *Pediatrics*, vol. 121, no. 2, pp. 449-450, 2008.

[7] M. S. Pearce, J. A. Salotti, and M. P. Little, "Radiation exposure from CT scans in childhood and subsequent risk of leukaemia and brain tumours: a retrospective cohort study," *Pediatr. Radiol.*, vol. 43, pp. 517-518, 2013.

[8] S. Mattsson, and S. Marcus, "Radiation dose management in CT, SPECT/CT and PET/CT techniques," *Radiat. Prot. Dosim.*, vol. 147, no. 1-2, pp. 13-21, 2011.

[9] R. Boellaard, M. J. O'Doherty, W. A. Weber, F. M. Mottaghy, M. N. Lonsdale, S. G. Stroobants, W. J. G. Oyen, *et al.,* "FDG PET and PET/CT: EANM procedure guidelines for tumour PET imaging: version 1.0," *Eur. J. Nucl. Med. Mol. Imaging*, vol. 37, pp.181-200, 2010.

[10] B. G. Wang, and Y. J. Qi, "PET image reconstruction using kernel method," *IEEE Trans. Med. Imaging*, vol. 34, no. 1, pp. 61-71, 2014.

[11] R. D. Schaart, "Physics and technology of time-of-flight PET detectors," *Phys. Med. Biol.*, vol. 66, no. 9, 2021.

[12] J. M. Geusebroek, A. W. M Smeulders, and J. Van De Weijer. "Fast anisotropic Gauss filtering," *IEEE Trans Image Process*, vol. 12, no. 08, pp. 938-943, 2003.

[13] C. Wang, Z. Hu, P. Shi, and H. Liu, "Low dose PET reconstruction with total variation regularization," *EMBC*, pp. 1917-1920, 2014.

[14] X. Yu, *et al.* "Low dose PET image reconstruction with total variation using alternating direction method" *PloS One*, pp.0166871, 2016.

[15] J. Dutta, Q. Li and R. M. Leahy, "Non-local means denoising of dynamic PET Images," *PloS One*, vol. 8, pp. 1-15, 2013.

[16] H. Arabi, and H. Zaidi. "Spatially guided nonlocal mean approach for denoising of PET images." *Med. Phys.*, vol. 47, no. 4, pp. 1656-1669, 2022.

[17] C. L. Yann, B. Yoshua and H. Geoffrey, "Deep learning," *NATUAS*, vol. 521, no. 7553, pp. 436-444, 2015.

[18] I. Goodfellow, Bengio, Y. Bengio and A. Courville, "Deep learning," *MIT Press.*, 2016.

[19] G. Kuang, J. H. Guan, K. Kim, X. Z. Zhang, J. Yang, Y. Seo, G. E. Fakhri, J. Y. Qi, and Q. Z. Li, "Iterative PET image reconstruction using convolutional neural network representation," *IEEE Trans. Med. Imaging*, vol. 8, no. 3, pp. 675-685, 2018.

[20] J. Xu, E. Gong, J. Pauly and G. Zaharchuk, "200x low-dose PET reconstruction using deep learning," *arXiv preprint arXiv:*1712. 04119, 2017.

[21] Z. Y. Peng, F. W. Zhang, J. Z. Sun, Y. Du, Y. Wang, and G. S. P. Mok, "Preliminary deep learning-based low dose whole body PET denoising incorporating CT information," *In IEEE NSS/MIC*, pp. 1-2, 2022.

[22] K. Gong, J. H. Guan, C. Liu, and J. Y. Qi, "PET image denoising using a deep neural network through fine tuning," *IEEE Trans. Radiat. Plasma Med. Sci*, vol. 3, no. 2, pp. 153-161, 2018.

[23] L. Zhou, J. D. Schaefferkoetter, I. W. Tham, G. Huang and J. Yan, "Supervised learning with cyclegan for low-dose FDG PET image denoising," *Med. Image Anal.,* vol. 65, pp.101770, 2020.

[24] S. Pan, E. Abouei, J. Peng, J. Qian, J. F. Wynne, T. Wang, C. Chang, *et al.,* "Full-dose PET synthesis from low-dose PET using 2D high efficiency denoising diffusion probabilistic model," *In Medical Imaging 2024: Clin. Biomed. Imaging*, vol. 12930, pp. 428-435, 2024.

[25] K. Gong, K. Johnson, G. E. Fakhri, Q. Li, and T. Pan, "PET image denoising based on denoising diffusion probabilistic model," *Eur. J. Nucl. Med. Mol. Imaging*, vol. 51, no. 2, pp. 358-368, 2024.

[26] C. Jiang, Y. Pan, M. Liu, L. Ma, X. Zhang, J. Liu, X. Xiong, and D. Shen, "PET-diffusion: Unsupervised PET enhancement based on the latent diffusion model," *In MICCAI*, vol. 14220, pp. 3-12, 2023.

[27] H. Xie, W. Gan, B. Zhou, M.K. Chen, M. Kulon, A. Boustani, X. Chen, Q. Liu, X. Guo, M. Xia, and L. Guo, "Dose-aware diffusion model for 3D low-dose PET denoising: A multi-institutional validation with reader study and real low-dose data," *Eur. J. Nucl. Med. Mol. Imaging*, 2024.

[28] L. Zhang, Z. Xiao, C. Zhou, J. Yuan, Q. He, Y. Yang, X. Liu, D. Liang, H. Zheng, W. Fan, and X. Zhang, "Spatial adaptive and transformer fusion network (STFNet) for low-count PET blind denoising with MRI," *Med. Phys.*, vol. 49, no. 1, pp. 343-356, 2022.

[29] Y. Luo, Y. Wang, C. Zu, B. Zhan, X. Wu, J. Zhou, D. Shen, and L. Zhou, "3D transformer-GAN for high-quality PET reconstruction," *In MICCAI*, vol. 12906, pp. 276-285, 2021.

[30] R. Hu and H. Liu, "TransEM: Residual Swin-transformer based regularized PET image reconstruction," *In MICCAI,* vol. 13434, pp. 184-193, 2022.

[31] A. Dosovitskiy, L. Beyer, A. Kolesnikov, D. Weissenborn, X. Zhai, T. Unterthiner, M. Dehghani, M. Minderer, G. Heigold, S. Gelly, *et al.,* "An image is worth 16x16 words: Transformers for image recognition at scale," *In ICLR*, 2021.

[32] S. Khan, M. Naseer, M. Hayat, S. W. Zamir, F. S. Khan, and M. Shah, "Transformers in vision: A survey," *ACM Comput. Surv. (CSUR),* vol. 54, no. 10, pp. 1-41, 2022.

[33] Z. Wang, X. Cun, J. Bao, and J. Liu, "Uformer: A general u-shaped transformer for image restoration," *In CVPR,* pp. 17683-17693. 2022.

[34] J. Liang, J. Cao, G. Sun, K. Zhang, L. V. Gool, and R. Timofte, "SwinIR: Image restoration using Swin transformer," *In ICCV Workshops,* pp. 1833-1844, 2021.

[35] D. Kingma, T. Salimans, B. Poole, and J. Ho, "Variational diffusion models," *NeurIPS,* vol. 34, no. 6, pp. 21696-21707, 2021.

[36] P. Dhariwal and A. Nichol, "Diffusion models beat Gans on image synthesis," *NeurIPS,* vol. 34, pp. 8780-8794, 2021.

[37] B. Xia, Y. Zhang, S. Wang, Y. Wang, X. Wu, Y. Tian, W. Yang, and L. Van Gool, "DiffIR: Efficient diffusion model for image restoration," *In ICCV*, pp. 13095-13105, 2023.

[38] D. Hendrycks and K. Gimpel, "Gaussian error linear units (GELUs)," *arXiv preprint arXiv:*1606. 08415, 2016.

[39] S. W. Zamir, A. Arora, S. Khan, M. Hayat, F. S. Khan, and M. H. Yang, "Restormer: Efficient transformer for high-resolution image restoration." *Proc. IEEE/CVF Conf. Comput. Vis. Pattern Recognit*., 2022.

[40] Y. Song, J. Sohl-Dickstein, D. P. Kingma, *et al.,* "Score-based generative modeling through stochastic differential equations," *Int. Conf. Learn. Represent*., 2020.

[41] J. Sun, Y. Du, C. Li, T. Wu, B. Yang, and G. SP Mok. "Pix2pix generative adversarial network for low dose myocardial perfusion SPECT denoising." *Quant. Imag. Med. Surg*., vol. 12, no. 7 pp. 3539, 2022.